Journal of Power Sources 313 (2016) 142–151

Contents lists available at ScienceDirect

Journal of Power Sources

journal homepage: www.elsevier.com/locate/jpowsour

High and rapid alkali cation storage in ultramicroporous carbonaceous materials

Young Soo Yun [a, b], Seulbee Lee [c], Na Rae Kim [c], Minjee Kang [d], Cecilia Leal [d], Kyu-Young Park [a], Kisuk Kang [a, e, **], Hyoung-Joon Jin [c, *]

[a] *Department of Materials Science and Engineering, Seoul National University, Seoul 151-742, South Korea*
[b] *Department of Chemical Engineering, Kangwon National University, Samcheok 245-711, South Korea*
[c] *Department of Polymer Science and Engineering, Inha University, Incheon 402-751 South Korea*
[d] *Department of Materials Science and Engineering, University of Illinois at Urbana–Champaign, Urbana, IL 61801, United States*
[e] *Center for Nanoparticles Research, Institute for Basic Science (IBS), Seoul National University, Seoul 151-742, South Korea*

HIGHLIGHTS

- Ultramicroporous carbonaceous materials (UCMs) were fabricated by a simple method.
- Alkali cations in ultramicropores delivered high capacitances even in high current rates.
- UCM-based symmetric supercapacitors showed notable electrochemical performances.

ARTICLE INFO

Article history:
Received 8 October 2015
Received in revised form
31 January 2016
Accepted 21 February 2016
Available online 4 March 2016

Keywords:
Ultramicropore
Activated carbon
Supercapacitor
Electrode
Energy storage

ABSTRACT

To achieve better supercapacitor performance, efforts have focused on increasing the specific surface area of electrode materials to obtain higher energy and power density. The control of pores in these materials is one of the most effective ways to increase the surface area. However, when the size of pores decreases to a sub-nanometer regime, it becomes difficult to apply the conventional parallel-plate capacitor model because the charge separation distance (*d*-value) of the electrical double layer has a similar length scale. In this study, ultramicroporous carbonaceous materials (UCMs) containing sub-nanometer-scale pores are fabricated using a simple in situ carbonization/activation of cellulose-based compounds containing potassium. The results show that alkali cations act as charge carriers in the ultramicropores (<0.7 nm), and these materials can deliver high capacitances of ~300 F g^{-1} at 0.5 A g^{-1} and 130 F g^{-1}, even at a high current rate of 65 A g^{-1} in an aqueous medium. In addition, the UCM-based symmetric supercapacitors are stable over 10,000 cycles and have a high energy and power densities of 8.4 Wh kg^{-1} and 15,000 W kg^{-1}, respectively. This study provides a better understanding of the effects of ultramicropores in alkali cation storage.

1. Introduction

Electrical double layer (EDL) capacitors, known as supercapacitors, have attracted much attention for energy storage applications because they can store large amounts of energy and deliver high power. The capability of EDL capacitors to supply high power stems from their rapid charge storage, which is reliant on the physical adsorption/desorption of a charge carrier without solid-state-diffusion [1–4]. The high energy is also attributed to the large interfacial areas of the electrode materials and the atomic-scale charge separation distances. The capacitance (C_{DL}) in EDL capacitors originates from a Stern-type compact double layer capacitance (C_H) in series with a diffuse layer capacitance (C_D) [2,3]. The C_{DL} can be expressed by the following equation: $\frac{1}{C_{DL}} = \frac{1}{C_H} + \frac{1}{C_D}$. Furthermore, the capacitance of EDL capacitors is conventionally assumed to be similar to that of a parallel-plate capacitor, i.e., $C = \frac{\varepsilon_r \varepsilon_0 A}{d}$, where ε_r is the electrolyte dielectric constant, ε_0 is the vacuum permittivity, *A* is the specific surface area of the electrode accessible to the electrolyte ions, and *d* is the effective thickness of the EDL (i.e., the Debye length)

---

* Corresponding author.
** Corresponding author. Department of Materials Science and Engineering, Seoul National University, Seoul 151-742, South Korea.
E-mail address: hjjin@inha.ac.kr (H.-J. Jin).

http://dx.doi.org/10.1016/j.jpowsour.2016.02.068
0378-7753/

[5–7]. However, recent studies have revealed that the parallel-plate capacitor model is insufficient to describe the electrochemical properties of nanoporous carbon-based EDL capacitors [8]. Huang et al. have reported the use of an electric double-cylinder capacitor (EDCC) model and an electric wire-in-cylinder capacitor (EWCC) model to describe mesoporous and microporous carbon electrodes, respectively [9,10]. These models provide good fits to experimental results, as reported by Simon and Gogotsi; in their work, an anomalous increase in the capacitance for pore sizes smaller than 1 nm and a slight increase in capacitance for pore sizes above 2 nm were observed in organic solvent based systems [11]. These results suggest that, in charge storage devices based on EDLs, pore size effects are critical to achieve high capacitance.

Numerous carbon-based electrode materials (CEMs) have been reported as electrodes for supercapacitors. The specific capacitances of these CEMs in aqueous electrolytes are highly variable, from 50 to ~286 F g^{-1} [12–21]. Wang et al. reported that a 3D few-layer graphene/multi-walled carbon nanotube hybrid nanostructures with a Brunauer-Emmett-Teller (BET) specific surface area of 743 m^2 g^{-1} showed a high specific capacitance of 286 F g^{-1} in KOH aqueous electrolyte [19]. This capacitance value is superior to that (223 F g^{-1}) of hierarchical porous carbon, which have a BET surface area of 2749 m^2 g^{-1} [20]. In addition, Liu et al. reported that flat-shaped graphene sheet-based supercapacitors can reach capacitances of 100–150 F g^{-1} in KOH electrolyte, while curved graphene-based supercapacitors showed ~250 F g^{-1} [21]. These reports suggest that the BET surface area and electroactive surface area can differ from each other. Therefore, design of effective porosity, with pores adapted to the appropriate electrolyte is crucial for the achievement of a high electroactive surface area and effective thickness of the EDL.

In water, alkali cations have relatively small hydrated ion sizes compared to organic cations such as tetraethylammonium (TEA). Conventionally, the electrolyte for EDLs has a high salt concentration of 6 M; in these concentrated solutions, alkali cations can be solvated by only 5–6 water molecules [22–24]. Therefore, at high salt concentrations, cations have a relatively small radius compared to fully hydrated cations, which have a radius of ~0.334 nm [25,26]. Therefore, the presence of ultramicropores smaller than 0.7 nm increases the capacitance for hydrated alkali cation storage, according to the EWCC model [11]. However, although previous reports have been made [27], the relationship between ultramicropores and capacitance/kinetics is not well understood for alkali cation storage. Thus, further studies on the relationship between the sub-nanometer scale pores and capacitance are required to improve the performance of supercapacitors.

In this study, we fabricated ultramicroporous carbon-based materials (UCMs) containing a large number of sub-nanometer pores by a controlled, in situ carbonization/activation process of cellulose-induced materials with potassium. Using UCMs as a platform, we investigated the interplay between half-nanometer-scale pores and the capacitance/kinetics of carbonaceous electrode materials. We found that the ultramicropores can store a remarkably high charge of ~300 F g^{-1}, and a specific capacitance of 130 F g^{-1} was achieved even at an extremely high current rate of 65 A g^{-1} by using alkali cations as charge carriers in aqueous media. This study provides a better understanding of the effects of ultramicropores in alkali cation storage and provides a description of a simple method of synthesizing UCMs.

2. Experimental

2.1. Preparation of aqueous dispersions of cellulose nanocrystals

Cotton cellulose powder (10 g, 20 μm, Sigma Aldrich) was hydrolyzed using 64 wt% aqueous H_2SO_4 solution (200 mL) (95%, OCI Company Ltd.). The mixture was stirred at 45 °C for 1 h, and then diluted with distilled water (200 ml). In order to remove the acid, the product was centrifuged at 25 °C for 15 min at a constant speed of 3000 rpm (Jouan, ISO9001, 1995/3777a). The hydrolyzed cellulose was separated from the suspension by centrifugation, and the acidic solution was discarded. The obtained cellulose nanocrystals (CNCs) were dialyzed against distilled water for several days using cellulose membrane dialysis tubing (M_w 11,124, Sigma Aldrich) until a neutral pH was obtained. Finally, the concentration of the aqueous dispersions of CNCs was adjusted to 1 wt%.

2.2. Preparation of UCM samples

KOH (0.5, 1, and 2 g) was added to an aqueous dispersion of CNCs (100 g). After stirring for 1 h, the CNC/KOH aqueous dispersions were frozen using dry ice (1 h). The samples were then immediately transferred to a lyophilizer (ALPHA 1–2 LD plus Fisher Bioblock Scientific, France) and freeze-dried at −50 °C and 0.0045 mbar for 72 h. The resulting yellow powders were thermally treated in a tube furnace by heating to 800 °C at a rate of 2 °C min^{-1} under flowing Ar at 200 mL min^{-1}. The resulting UCM samples were washed with distilled water and ethanol several times and transferred to a vacuum oven for storage at 30 °C.

2.3. Electrochemical characterization

Electrochemical measurements were performed using a three-electrode system with Ag/AgCl and Pt as reference and counter electrodes, respectively, and a two-electrode system composed of symmetric active materials in a beaker cell. For electrode preparation, 5 wt% polytetrafluoroethylene (PTFE, Sigma-Aldrich, 60 wt% dispersion in H_2O) was added to the UCM samples as a binder. Typically, the UCM samples and PTFE were mixed into a paste using a mortar and pestle, rolled into uniformly thick sheets (thicknesses ranged from 40 to 50 μm), and punched into 1 cm diameter electrodes. The electrodes had weights of between 3 and 4 mg after drying overnight at 100 °C. Aqueous solutions of 0.5, 2, and 6 M KOH and 0.5 M K_2SO_4 were used as electrolytes to investigate the potassium ion storage behavior. In addition, 0.5, 2, and 6 M NaOH and 0.5 M Na_2SO_4 aqueous solutions were used as electrolytes to investigate sodium ion storage behavior, and 2 M LiOH and 0.5 M Li_2SO_4 aqueous solutions were used as electrolytes to study lithium ion storage behavior. Electrochemical data were obtained using cyclic voltammetry, chronopotentiometry, and electrical impedance spectroscopy (EIS) (PGSTAT302N, Autolab). Capacitance, energy density, and power density were all characterized by galvanostatic measurements. The specific capacitance of the symmetric supercapacitors was determined from the galvanostatic measurements using the equation

$$C = \frac{4I_{cons}}{mdV/dt}, \tag{1}$$

where I_{cons} is the (constant) current, m is the total mass of both carbon electrodes, and dV/dt was calculated from the slope of the discharge curve over the range from $V = V_{max}$ (the voltage at the beginning of discharge) to $V = ½V_{max}$. The specific power density and energy density of the supercapacitors were also calculated as follows:

$$P = \Delta V \times I/m, \tag{2}$$

$$E = P \times t/3600\ ,\ \text{and} \tag{3}$$

$$\Delta V = (E_{max} + E_{\min})/2. \tag{4}$$

In Equations (2)–(4), $E_{\max}$ and $E_{\min}$ are the potentials at the beginning and the end of discharge (in V), respectively, I is the charge/discharge current (in A), t is the discharge time (in s), and m is the total mass (in kg) of the active materials, including both electrodes, in the symmetric supercapacitors.

2.4. Characterization

The morphologies of the prepared samples were examined using field-emission transmission electron microscopy (FE-TEM, JEM2100F, JEOL, Tokyo, Japan). The chemical compositions of the samples were evaluated using X-ray photoelectron spectroscopy (XPS, PHI 5700 ESCA, Chanhassen, MN, USA) with monochromatic Al Kα radiation ($h\nu = 1486.6$ eV). X-ray diffraction (XRD, Rigaku DMAX 2500) analysis was performed using Cu-Kα radiation (with a wavelength $\lambda = 0.154$ nm) at 40 kV and 100 mA. Fourier transform infrared spectroscopy (FT-IR) was performed using a VERTEX 80v (Bruker Optics, Germany). Raman spectra were recorded using a continuous wave, linearly polarized laser with a wavelength of 514 nm, a 50-μm pinhole, and a 600-groove/mm grating. To ensure nondestructive measurements, a low laser power of <300 μW was used to irradiate the samples. In addition, the BET specific surface area and differential pore volumes were determined from nitrogen adsorption/desorption isotherms (ASAP 2020, Micromeritics, Norcross, GA, USA) at −196 °C. The BET surface areas were calculated according to BET theory, and the micropore surface areas were obtained using t-plot theory. Ultramicropore size distributions by DFT method were investigated by CO_2 adsorption at 273 K using a volumetric sorption analyzer (ASAP 2020, Micromeritics, USA). CO_2 adsorption isotherms were measured in the pressure range 0.019–794 mmHg. Prior to the adsorption measurements the samples were degassed for 18 h at 393 K under vacuum. Small angle X-ray scattering (SAXS) experiments were conducted using custom built equipment (with help of Forvis Technologies, Santa Barbara) composed of a Xenocs GeniX3D CuKα Ultra Low Divergence X-ray source (1.54 Å/8 keV), with a divergence of 1.3 mrad. The 2D scattering data were recorded on a Pilatus 300 K 20 Hz hybrid pixel Detector (Dectris). A sample-to-detector distance was chosen to cover an overall range of momentum transfer wave vectors $0.01\ \text{Å}^{-1} < q < 1\ \text{Å}^{-1}$, and the equipment was calibrated using a silver behenate powder standard. The average acquisition time for each sample was 1 h and the measured data were corrected for background scattering. The 2D datasets were converted into 1D scattering curves (intensity versus wave vector q) using a Fit2d software. The scattering curves were analyzed based on a unified fit model using the IRENA tool (v. 2.58). The unified fit model describes a complex structure in terms of structural levels, where each level is composed of a Guinier part and a tail described by a power law.

3. Results and discussion

3.1. Synthesis of UCMs

Activated carbon materials are conventionally fabricated from polymer precursors by carbonization, followed by activation. When sufficient heat is applied to the polymer in an inert atmosphere, pyrolysis of the polymer precursors begins, breaking down the C–C bonds of the polymer backbone. The chain is then transformed into a conjugated hexagonal carbon structure [28]. Previous researchers have suggested that activation of the polymeric carbon with KOH occurs via two main mechanisms [29]. The first step is the consumption of carbon by oxygen, which is catalyzed by alkali metals below 700 °C, producing carbon monoxide and carbon dioxide. The second activation mechanism occurs above 700 °C and is accompanied by the formation of metallic potassium. This metallic potassium penetrates into the graphitic layers formed by pyrolysis and results in numerous topological defects and the expansion of the graphitic lattice by the rapid removal of the intercalated potassium. Ultramicropores are likely to form due to the expansion of the lattice during this second activation step. In our modified activation process, KOH is introduced to CNCs to maximize the

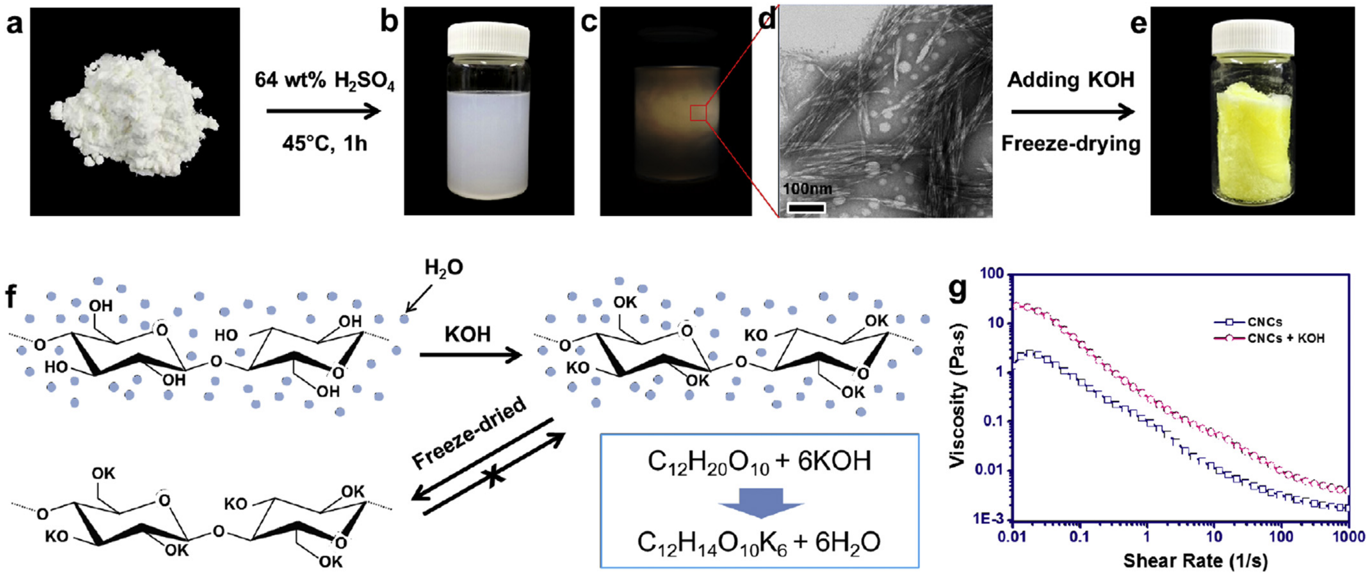

Fig. 1. Photographs of a) cotton cellulose powder and b) aqueous dispersions of CNCs. c) Birefringence image of aqueous dispersions of CNCs. d) FE-TEM image of CNCs, and e) optical image of cellulose-based carbon precursors containing potassium (yellow cryogel, $C_{12}H_{14}O_{10}K_6$). f) Schematic process for preparing the yellow cryogel. g) Shear viscosity versus shear rate curve of aqueous dispersions of CNCs (blue rectangles) and aqueous dispersions of CNCs with KOH (pink circles). (For interpretation of the references to color in this figure legend, the reader is referred to the web version of this article.)

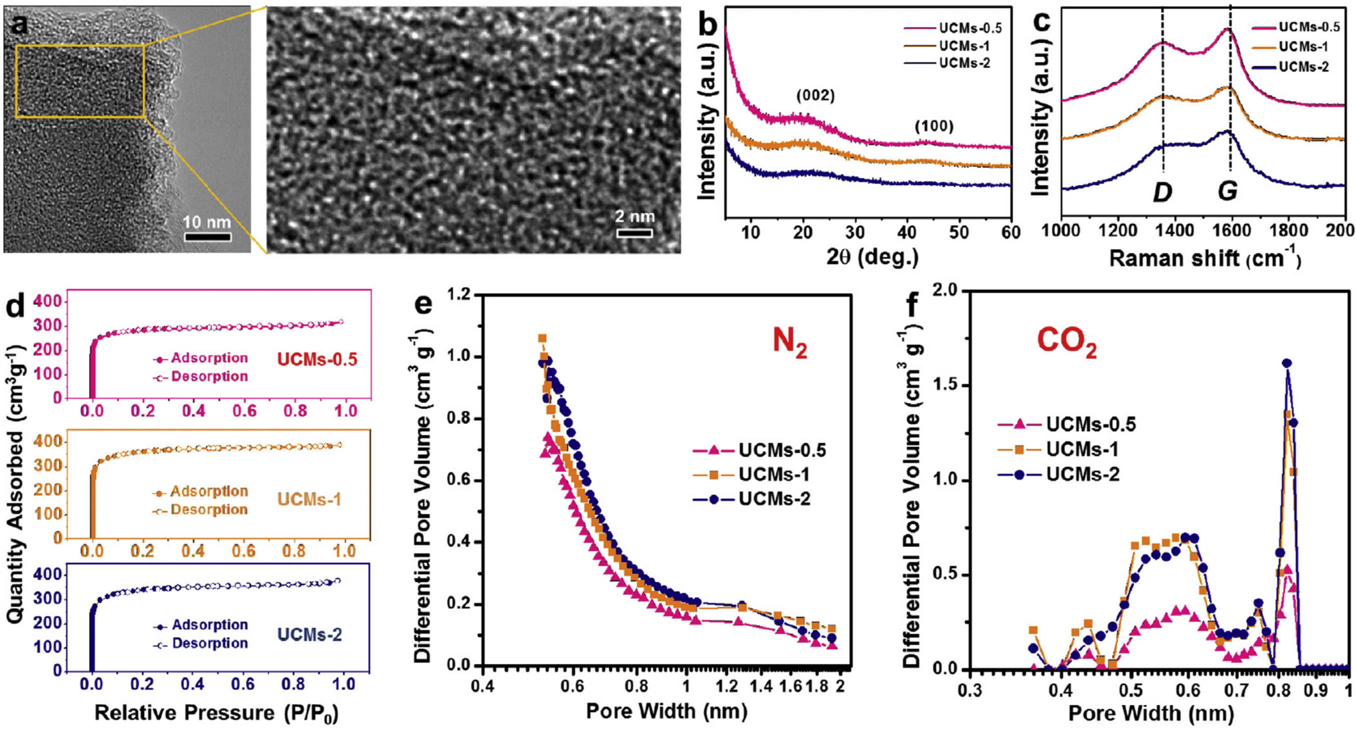

Fig. 2. a) FE-TEM image of UCM-1 with different magnifications. b) XRD data and c) Raman spectra of UCM samples. d) Nitrogen adsorption and desorption isotherm curves of UCM samples. Pore size distributions of UCM samples characterized by e) nitrogen and f) carbon dioxide adsorption/desorption methods.

second step caused by the presence of potassium (Fig. 1a–e). The CNCs serve as Lewis acids in basic media; thus, the addition of KOH induces ion exchange between H^+ and K^+ in the CNCs, ensuring an atomic level of dispersion of potassium (Fig. 1f). In this process, the CNCs are dissolved by the KOH, as confirmed by an increase in the solution viscosity (Fig. 1g). The reaction can be expressed as $C_{12}H_{20}O_{10} + 6KOH \rightarrow C_{12}H_{14}O_{10}K_6 + 6H_2O$, which corresponds to a 1:1 weight ratio of CNCs:KOH (Fig. 1f). Subsequent water removal by freeze-drying results in the formation of a yellow cryogel (mainly $C_{12}H_{14}O_{10}K_6$) (Fig. 1e). The cryogel was then thermally treated at 800 °C for in situ carbonization/activation, resulting in UCM-1 as a targeted product material (here, “1” in UCM-1 refers to the weight ratio of KOH to CNCs, and this method of sample designation is also used for other samples; e.g., UCM-2).

3.2. Material properties of UCMs

The morphology of UCM-1 was observed using FE-TEM (Fig. 2a). High-resolution FE-TEM shows a highly amorphous carbon structure with a rough surface. Harris and co-workers have proposed that micropores in sucrose-induced chars are caused by fullerene-like curved and twisted elements [30]. Other researchers have pointed out that fullerene-like elements are analogous to the so-called random schwarzite structure, which has a negative curvature induced by topological carbon defects [31–33]. Thus, micropores mainly form as closed pores by random aggregation of the concave and convex surfaces. In this case, the empty spaces left between the fullerene-like fragments may have a random shape rather than the slit-like shapes observed previously [29].

Table 1
Textural properties of UCM samples characterized by nitrogen adsorption and desorption tests.

Sample name	Surface area (m^2 g^{-1})		Pore volume (cm^3 g^{-1})	
	Total	t-plot	Total	t-Plot
UCM-0.5	996.1	971.8	0.49	0.44
UCM-1	1267.2	1252.1	0.60	0.57
UCM-2	1199.9	1178.7	0.59	0.54

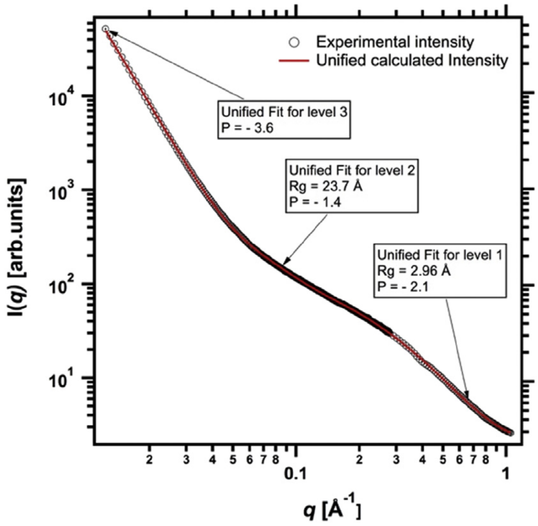

Fig. 3. Small angle X-ray scattering (SAXS) profile for UCM-1. The unified fit model by Beaucage was used to fit (red solid line) the experimental scattering data (hollow circles). The complex structure of UCM-1 was hierarchically divided into three sub-structural levels where each level is composed of a Guinier and structurally limited power law. Information regarding the particle size (radius of gyration, R_g) and sample morphology can be obtained from Guinier fits and Porod exponents (P), respectively. (For interpretation of the references to color in this figure legend, the reader is referred to the web version of this article.)

Simultaneously, chemical activation using KOH promotes the development of slit-like pores due to the expansion of graphitic lattice. As a result, the numerous closed pores can open, which induces a dramatic increase in the surface area. The differences in contrast in the high-resolution FE-TEM image shown in Fig. 2a can originate from the numerous topological defects, nanopores, and random orientations of the fullerene-like fragments present in UCM-1.

The amorphous carbon structure was characterized by XRD and Raman spectra (Fig. 2b and c). Broad graphitic (002) and (100) peaks are present in the XRD data of UCM-1, indicating that the hexagonal graphene layers are not well-stacked (Fig. 2b). Other samples with different cellulose to KOH weight ratios also show similar carbon structures with poorly developed graphitic structures (Fig. 2b). In contrast, the Raman spectrum of UCM-1 clearly shows the main *D* and *G* bands (Fig. 2c). The *D* band represents the intrinsic phonon mode with A_{1g} symmetry of the infinite aromatic

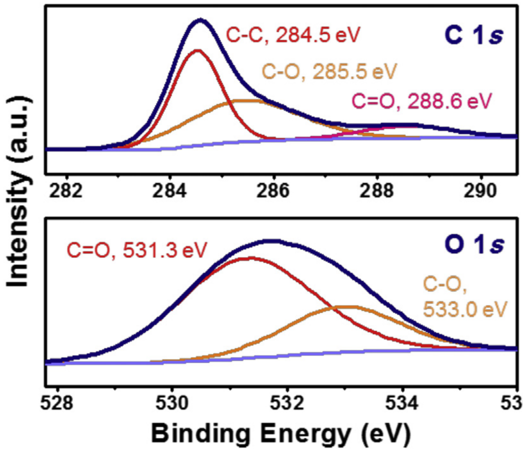

Fig. 4. XPS a) C 1s and b) O 1s spectra of UCM-1.

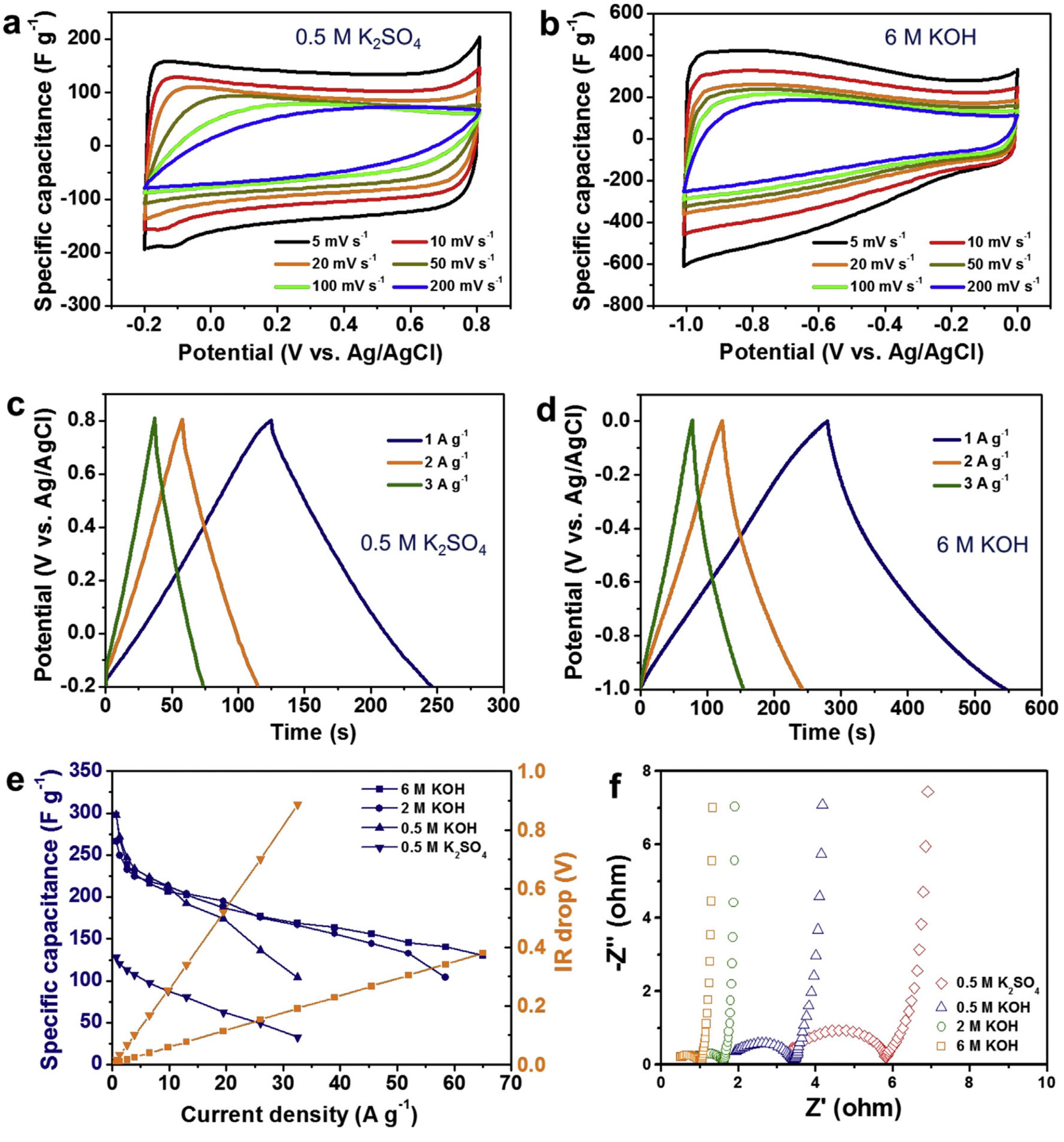

Fig. 5. Cyclovoltammograms of UCM-1 in a) 0.5 M K_2SO_4 aqueous electrolyte and b) 6 M KOH aqueous electrolyte. Galvanostatic charge/discharge profiles of UCM-1 in c) 0.5 M K_2SO_4 aqueous electrolyte and d) 6 M KOH aqueous electrolyte. Rate capabilities of UCM-1 at different current densities in e) various KOH and K_2SO_4 aqueous electrolytes. f) Nyquist plots of UCM-1 in various KOH and K_2SO_4 aqueous electrolytes.

ring that is activated by the structural disorder, and the *G* band reflects the hexagon structure related to the E_{2g} vibration mode of the sp^2-hybridised C atoms. The I_D/I_G intensity ratio of UCM-1 is about 0.8, which is similar to those of UCs-0.5 and UCM-2 (Fig. 2c), indicating that the ordered hexagonal structure is several nanometers in size. These suggest that the amorphous carbon structure of UCM-1 is composed of numerous nanometer-sized crystallites with random orientations. The results also correspond to the carbon structure of typical activated carbon, which contains a certain two-dimensional order but no three-dimensional graphitic ordering [34].

The pore structure of our samples was characterized using nitrogen adsorption and desorption isotherm analysis. The isotherm curve reveals that the UCM samples have an IUPAC type-I microporous structure (Fig. 2d), and most of the pore sizes are less than 0.7 nm (Fig. 2e). The BET specific surface areas of UCM-0.5, –1, and –2 are 996.1 $m^2\ g^{-1}$, 1267.2 $m^2\ g^{-1}$, and 1199.9 $m^2\ g^{-1}$, respectively. Approximately 98% of the overall surface area consists of the t-plot micropore area. Single point adsorption total pore volumes are 0.49, 0.60, and 0.59 $cm^3\ g^{-1}$ in UCM-0.5, –1, and –2, respectively, and the corresponding micropore volumes are 90% (0.44 $cm^3\ g^{-1}$), 95% (0.57 $cm^3\ g^{-1}$), and 92% (0.54 $cm^3\ g^{-1}$), respectively. These high micropore volume ratios (mainly composed of ultramicropore volume) indicate that there are only a few meso- and macropores, and the chemical activation by atomically dispersed potassium successfully contributed to the development of ultramicropores. The ultramicropores (<0.7 nm) are further characterized by CO_2 adsorption and desorption isotherm analysis. As shown in Fig. 2f, the differential pore volumes (DPVs) and the distribution of these pore volumes are similar in all the UCM samples. DPVs between approximately 4 and 7 Å are dominant. In contrast, the total quantities of DPVs in UCM-1 and UCM-2 are larger than those in UCM-0.5. The textural properties of the UCM samples are provided in Table 1.

As shown in Fig. 3, the microstructure of UCM-1 was further investigated by the SAXS data which depicts a log-log plot of scattering intensity as a function of q for UCM-1. Multiple exponential and linear decay regions are shown in the SAXS scattering curve, indicative of the multi-size-scale structure. The scattering behavior of UCM-1, originating from the multiple length scales, can be analyzed using the unified fit model proposed by Beaucage [35]. The unified model considers scattering from the complex structure as the summation of scattering from structural levels. Each structural level is described by an exponential regime (Guinier) and an associated linear power-law regime (Porod) in a log-log form. The model is especially suited for describing multi-scale scattering because it can distinguish Guinier regimes buried between two power-law regimes [36]. Three structural levels were derived from the unified model fit. The power law scattering behavior at low q ($0.01 < q < 0.07$ Å^{-1}), with a slope of -3.6, indicates that the primary particles (hexagonal carbon layers) are aggregated into clusters with rough surfaces. For $0.07 < q < 0.5$ Å^{-1}, the scattering from primary particles is presented with the Guinier regime yielding a radius of gyration ($R_g = 23.7$ Å) and the Porod regime, yielding a slope of -1.4. The information regarding a substructural dimensionality of scatterers can be obtained from the Porod exponent. The suggested overall particle shape from the Porod exponent is considered to be intermediate between 2D leaflet-like and 1D rod-like. The smallest structural level at high q regime ($0.5 < q < 1.0$ Å^{-1}) shows the power-law scattering with an exponent of 2.1 and Guinier scattering that corresponds to an average pore size $R_g = 2.96$ Å. Assuming that the pores have a 2D leaflet-like shape inferred from the exponent 2.1, the value of $R_g = 2.96$ Å translates into a mean thickness of D = 5.92 Å according to [$D \approx 2R_g$] [37]. The effective pore size obtained by SAXS measurements is in agreement with the results from BET and CO_2 adsorption/desorption experiments.

The surface properties of UCM-1 were investigated by XPS (Fig. 4). Several peaks (i.e., C—O and C═O bonds centered at 285.5 and 288.6 eV, respectively) were observed along with that of the main C—C bond centered at 284.5 eV in the XPS C 1*s* spectrum (Fig. 4a). Also, two distinct peaks centered at 531.3 and 533.0 eV were found in the XPS O 1*s* spectrum, indicating that UCM-1 contains oxygen functional groups on the surface (Fig. 4b). The observed C/O ratio is 10.1 for UCM-1, which is similar to those of UCM-0.5 and UCM-2, 10.8 and 10.2, respectively. FT-IR spectra of the UCM samples also reveal that they exhibit comparable surface properties (Figure S1).

3.3. Electrochemical properties of UCMs

The electrochemical properties of UCM-1 were investigated in various aqueous electrolytes using a half-cell configuration with Ag/AgCl and Pt as reference and counter electrodes, respectively. The equilibrium potential (open circuit voltage, OCV) was found to

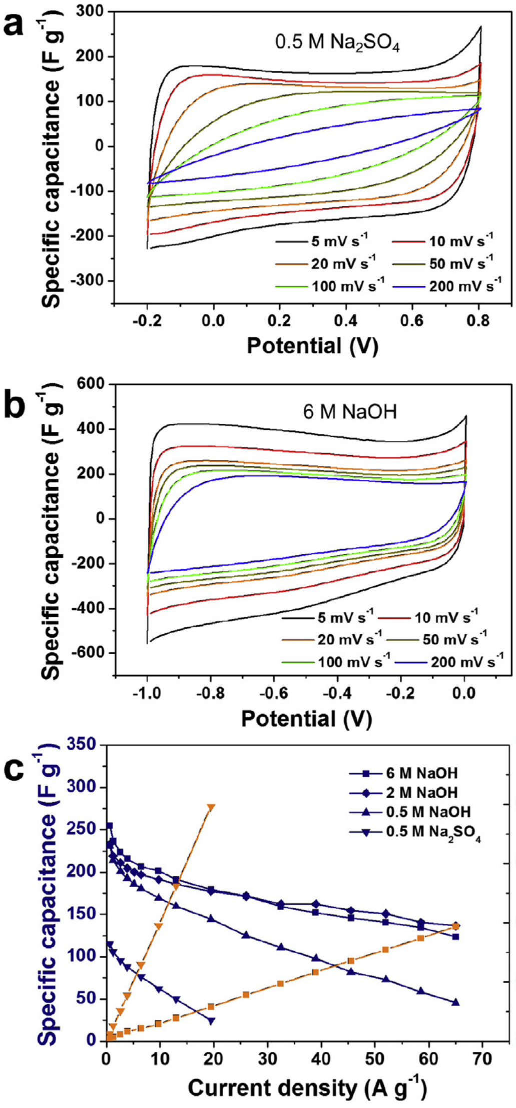

Fig. 6. Cyclovoltammograms of UCM-1 in a) 0.5 M Na_2SO_4 aqueous electrolyte and b) 6 M NaOH aqueous electrolyte. c) Rate capabilities of UCM-1 in various NaOH and Na_2SO_4 electrolytes.

be −0.12 V vs. Ag/AgCl, and UCM-1 was tested at two different operating potentials, −0.2–0.8 V and 0.0 to −1.0 V vs. Ag/AgCl, in which the charge carriers were sulfate anions and alkali cations, respectively. The cyclovoltammogram of UCM-1 in a 0.5 M K_2SO_4 aqueous electrolyte had a rectangular shape at a scan rate of 5 mV s^{-1} in a potential range of −0.2 to 0.8 V vs. Ag/AgCl (Fig. 5a). This result indicates ideal capacitive behavior and physical adsorption and desorption of the solvated anions (hydrated SO_4^-). The steep slopes of the current changes at the switching potentials indicate a small anion storage mass-transfer resistance. However, the rectangular shapes gradually change to oval shapes at higher scan rates, indicating an increase in the mass-transfer resistance. In contrast, cyclovoltammograms of UCM-1 in a 6 M KOH aqueous electrolyte measured over a potential range varying from 0 to −1 V vs. Ag/AgCl show a continuous increase in the capacitance over a broad potential range, from −0.2 V to −1 V (Fig. 5b). The capacitance was found to be as high as 312 F g^{-1}; that is, 2–3 times greater charge was stored at the same current density when potassium ions were used as charge carriers. Moreover, at relatively high scan rates, the cyclovoltammograms for potassium ion storage maintained their initial shapes with little distortion, indicating superior rate performance.

Galvanostatic charge/discharge profiles of UCM-1 show results consistent with those observed in the cyclovoltammograms (Fig. 5c and d). Galvanostatic charge/discharge profiles in a 0.5 M K_2SO_4 aqueous electrolyte exhibited linear charge/discharge behavior, indicating ideal capacitive character. Profiles in a 6 M KOH aqueous electrolyte were similar, with a slight alteration of the slope but with remarkably higher capacitance. Part of the extra capacitance can be attributed to pseudocapacitive cation storage on the oxygen functional groups. Specific capacitances and *IR* drop values of UCM-1 under various current densities are shown in Fig. 5e. In 6 M KOH aqueous electrolyte, the specific capacitance was 300 F g^{-1} at a current density of 0.5 A g^{-1}, which is about 2–3 times higher than the value of 122 F g^{-1} observed in 0.5 M K_2SO_4 aqueous electrolyte. This large capacitance gap between K^+ and SO_4^- storages may be caused by the additional pseudocapacitive charge storage and pore size effects. As shown in Fig. 5e, at current densities below 3 A g^{-1}, the specific capacitances increased by 60 F g^{-1}, which could originate from the pseudocapacitive effects in oxygen atoms [38–40]. In addition, the hydrated sulfate anion and potassium cation radii are 7.33 Å and 3.34 Å, respectively; thus, the hydrated sulfate anion is likely to be too large to be stored in the ultramicropores. The ionic radius of a bare sulfate anion is 2.90 Å (5.80 Å in diameter) based on the Pauling model, suggesting that only a small portion of the ultramicropores can be used to store sulfate anions after desolvation. Therefore, the capacitance gap of approximately 130 F g^{-1} (except ~60 F g^{-1} by pseudocapacitance) could be due to differences between the pore size and the hydrated ion size. From a quantitative standpoint, more potassium ions can be stored in the ultramicropores than sulfate anions because of their smaller size. Additionally, the relatively small *d*-value of potassium ions leads to an increase in capacitance, because capacitance and *d*-value have an inverse relationship according to the following equation, $C = \frac{\varepsilon_r \varepsilon_0 A}{d}$. Thus, the ultramicropores are highly effective for capacitive charge storage of alkali cations.

To confirm the relationship between electrolyte concentration and specific capacitance, the same electrochemical tests were performed in 0.5 M and 2 M KOH aqueous electrolytes (Fig. 5e). The specific capacitance in a 2 M KOH aqueous electrolyte is ~300 F g^{-1} at a current density of 0.5 A g^{-1}, which is similar to that observed in 6 M KOH aqueous electrolyte. In a 0.5 M KOH aqueous electrolyte, the specific capacitance is ~267 F g^{-1} at the same current density, indicating that the change in the solvated ion size slightly affects the specific capacitance at different salt concentrations. In addition, the relatively low ionic conductivity of the 0.5 M KOH electrolyte may contribute to the slightly lower performance at higher current densities due to high concentration polarization. It is notable that UCM-1 shows a high capacitance (130 F g^{-1}) at a current density of 65 A g^{-1} in 6 M KOH electrolyte. This result means that the

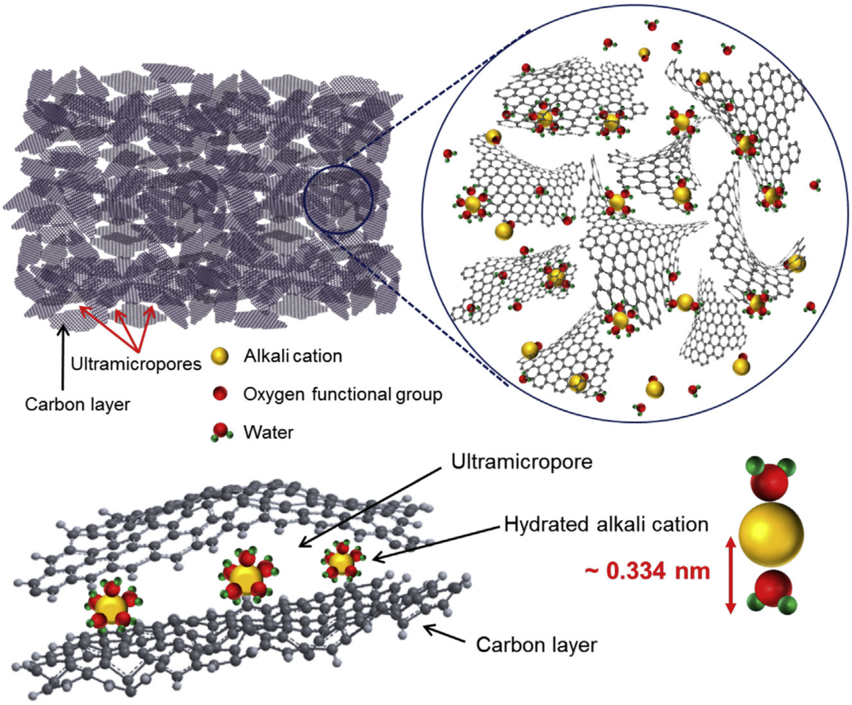

Fig. 7. Schematic model for hydrated alkali cation storage in UCM samples. The hydrated alkali cations in ultramicropores interact with all the carbon walls on every side, and they have a very small d-value that has a maximum at ~0.334 nm.

ultramicropores do not impede the fast potassium ion storage behavior. Nyquist results for UCM-1 in the various solvent systems support this claim, as shown in Fig. 5f. The equivalent series resistance (ESR) of UCM-1 in 6 M KOH aqueous electrolyte is ~1 Ω, smaller than those of the others. Also, the ionic resistance is larger in 0.5 M K_2SO_4 than in 0.5 M KOH aqueous electrolyte. This result suggests that potassium ion storage in ultramicropores provides excellent kinetic performance.

This was confirmed in similar experiments using sodium ions as charge carriers, where cyclovoltammograms of UCM-1 in 0.5 M Na_2SO_4 and 6 M NaOH aqueous electrolytes show results consistent with those in 0.5 M K_2SO_4 and 6 M KOH aqueous electrolytes, as shown in Fig. 6a and b. However, rate performance of UCM-1 in NaOH aqueous electrolytes is superior to that in KOH electrolytes (Fig. 6c). Although specific capacitances of UCM-1 in NaOH electrolytes are approximately 60 F g^{-1} lower than those in aqueous KOH electrolytes, a specific capacitance of 137 F g^{-1} is achieved at a current density of 65 A g^{-1} in a 6 M NaOH electrolyte. High capacitance and superior rate performance were also observed when using Li ions as a charge carrier (Figure S2), indicating that the high and rapid alkali cation storage in aqueous electrolyte is not related to the specific alkali cation used. Also, the electrochemical performance of UCM-1 are superior to those of previously reported materials [12–21].

In addition, UCM-0.5 and UCM-2 show high capacitance and outstanding rate performances. As shown in Fig. 2f, the DPV distributions of UCM-0.5, UCM-1, and UCM-2 are similar; however, the BET specific surface areas of UCM-1 is higher than those of UCM-0.5 and UCM-2. These results indicate that the UCM samples have similar pore structures but different the number of pores differs. Therefore, the UCM samples showed some differences in their specific capacitances but had similar rate capabilities [Fig. 5(e) and S3].

3.4. Charge storage behavior in UCMs

Fig. 7 shows a schematic model of the alkali cation storage behavior in UCM-1. Alkali cations hydrated by several water molecules can be stored in ultramicropores created from the randomly aggregated nanometer-scale hexagonal carbon fragments. In this case, the charged hydrated cations in the ultramicropores interact with the carbon walls on all sides, indicating that the conventional

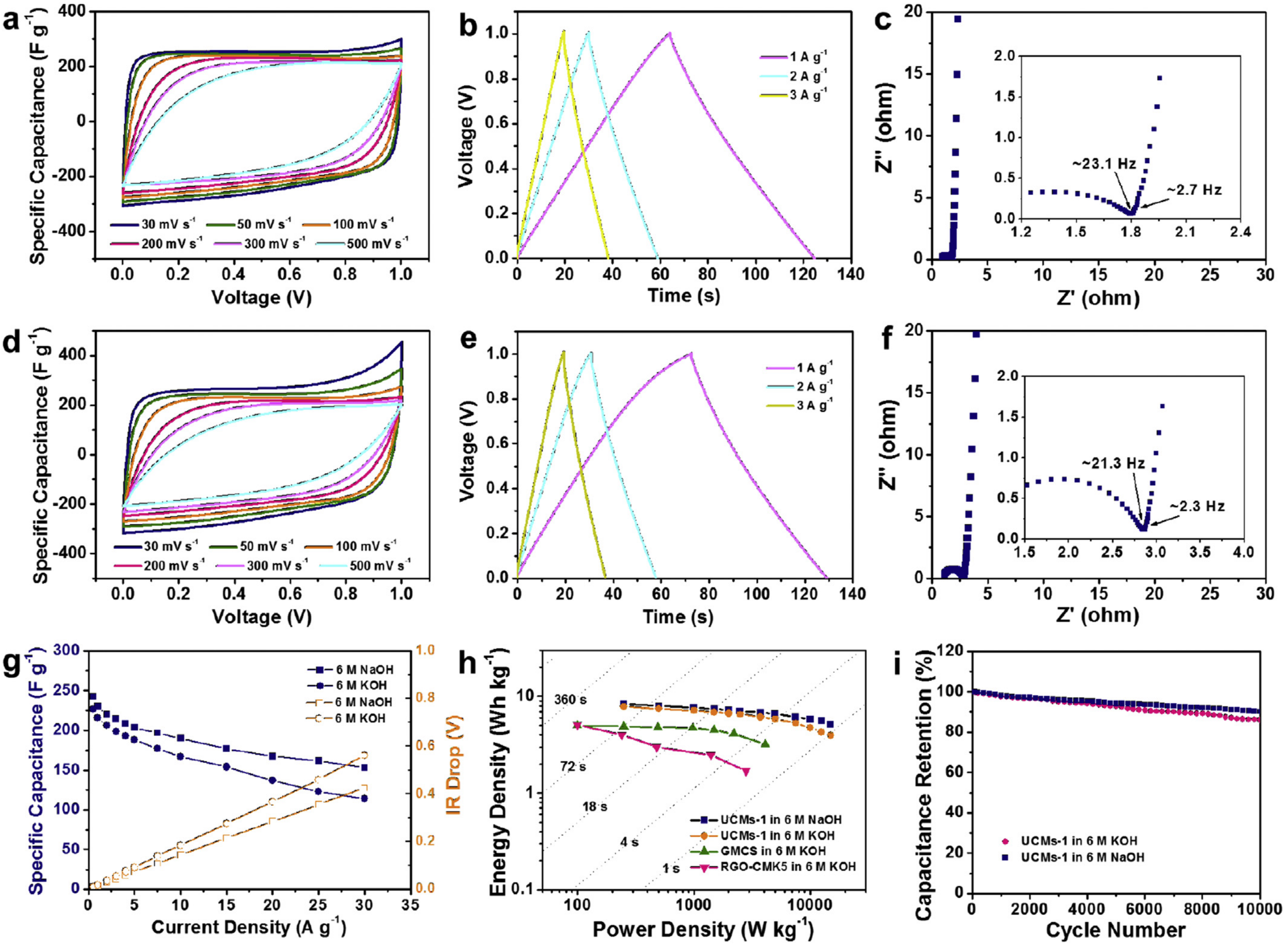

Fig. 8. Electrochemical performance results of symmetric UCM-1-based supercapacitors. a) Cyclovoltammograms at various scan rates, b) galvanostatic charge/discharge profiles at different current densities, and c) Nyquist plot in 6 M NaOH aqueous electrolyte. d) Cyclovoltammograms at various scan rates, e) galvanostatic charge/discharge profiles at different current densities, and f) Nyquist plot in 6 M KOH aqueous electrolyte. g) Rate capabilities in 6 M NaOH and KOH aqueous electrolytes at different current densities. h) Ragone plots of UCM-1-based supercapacitors in 6 M NaOH electrolyte (navy rectangular) and in 6 M KOH (orange circle) compared to literature data including: graphene-mesoporous carbon spheres (GMCS, olive triangle) [41], and graphene-CMK-5 (pink inverse triangle) [42]. i) Capacitance retention over 10,000 charge/discharge cycles of UCM-1-based supercapacitors at a current density of 2 A g^{-1}. (For interpretation of the references to color in this figure legend, the reader is referred to the web version of this article.)

parallel-plate capacitor model is not well fitted for charge storage in ultramicropores. The specific capacitance increases proportionally with a reduction in d-value (below 0.334 nm of potassium ions), and the charge adsorption/desorption kinetics are mostly surface-controlled. In this respect, by using hydrated alkali cations as charge carriers in an aqueous electrolyte system, ultramicropores can contribute to the specific capacitance of carbon-based electrodes without loss of rate performance. In addition, the pseudocapacitive behavior of oxygen functional groups in the carbon edge sites further increase the specific capacitance.

3.5. Electrochemical performance in full cells

Full cell tests of UCM-1 were performed in 6 M NaOH and 6 M KOH aqueous electrolytes using a symmetric configuration. The supercapacitors in 6 M NaOH aqueous electrolyte yielded rectangular cyclovoltammograms (Fig. 8a) and linear galvanostatic charge/discharge profiles (Fig. 8b) at different scan rates and current densities, respectively. The high-power characteristics were further investigated by means of Nyquist plots in the frequency range of 100 kHz to 0.1 Hz, as shown in Fig. 8c. The vertical line in the low-frequency region represents the ideal capacitive behavior of the UCM-1-based supercapacitors in 6 M NaOH aqueous electrolyte. The magnified data in the inset of Fig. 8c shows that the transition region associated with the migration of the electrolyte between the RC semicircle and the vertical line is small, indicating that Warburg resistance is minimal. This corresponds to an ESR of 1.8 Ω, which is similar to that of the other carbonaceous-material-based supercapacitors [41,42]. The same tests of UCM-1-based supercapacitors in a 6 M KOH aqueous electrolyte showed similar results, as shown in Fig. 8d and e. However, the overall performance is slightly worse than that in a 6 M NaOH aqueous electrolyte. Specific capacitances of the UCM-1-based supercapacitors are calculated to be 242.4 F g^{-1} and 226.5 F g^{-1} in 6 M NaOH and 6 M KOH aqueous electrolytes, respectively, at a current density of 0.5 A g^{-1}, and they are 153.2 F g^{-1} and 114 F g^{-1} at a current rate of 30 A g^{-1} (Fig. 8g). These capacitance values are much higher than other carbon-based and different type of electrolyte-based supercapacitors [Figures S4-6]. Ragone plots show that the UCM-1-based supercapacitors have high energy and power characteristics, reaching 8.4 Wh kg^{-1} and 15,000 W kg^{-1}, respectively (Fig. 8h). These values are higher than those of other carbon-based supercapacitors in 6 M KOH aqueous electrolytes [29,30]. The UCM-1-based supercapacitors exhibit stable cycles over 10,000 charge/discharge cycles at a current density of 2 A g^{-1} (Fig. 8i). Furthermore, capacitance retention values of 90.1% and 86.1% were achieved after 10,000 cycles.

4. Conclusion

We fabricated the UCM samples by means of an in situ carbonization/activation process using cellulose-based compounds with atomically dispersed potassium. The UCM samples had an amorphous carbon structure composed of several nanometer-scale hexagonal carbon fragments, in which well-developed ultramicropores of approximately 4 and 7 Å were observed. The specific surface areas of UCM-0.5, −1 and −2 were 996.1 m^2 g^{-1}, 1267.2 m^2 g^{-1}, and 1199.9 m^2 g^{-1}, respectively, and they had micropore volume ratios of >90%. The UCM samples showed outstanding capacitances of ~300 F g^{-1} and excellent rate performance (130 F g^{-1} at 65 A g^{-1}) when alkali cations were used as charge carriers in an aqueous electrolyte. UCM-1-based symmetric supercapacitors delivered a high energy of 8.4 Wh kg^{-1} and a high power of 15,000 W kg^{-1} with stable cycling performance in aqueous electrolytes. These results provide a new insight into the role of sub-nanometer pores in the electrode and a feasible strategy for their utilization in supercapacitor electrodes.

Acknowledgments

This work was supported by the Industrial Strategic Technology Development Program, (Project No. 10050477, Development of separator with low thermal shrinkage and electrolyte with high ionic conductivity for Na-ion batteries) funded by the Ministry of Trade, Industry and Energy. This work was supported by a grant from the Technology Development Program for Strategic Core Materials funded by the Ministry of Trade, Industry & Energy, Republic of Korea (Project No. 10050858) and also supported by the Energy Efficiency & Resources of the Korea Insitute of Energy Technology Evaluation and Planning (KETEP) grant funded by the Korea government Ministry of Trade, Industry&Energy (MOTIE) (No. 20132020000270).

Appendix A. Supplementary data

Supplementary data related to this article can be found at http://dx.doi.org/10.1016/j.jpowsour.2016.02.068.

References

[1] P. Simon, Y. Gogosi, Materials for electrochemical capacitors, Nat. Mater. 57 (2008) 845–854.
[2] L.L. Zhang, X.S. Zhao, Carbon-based materials as supercapacitor electrodes, Chem. Soc. Rev. 38 (2009) 2520–2531.
[3] M. Lu, Supercapacitors: Materials, Systems and Applications, Wiley-VCH, Weinheim, Germany, 2013.
[4] Y.S. Yun, G. Yoon, K. Kang, H.J. Jin, High-performance supercapacitors based on defect-engineered carbon nanotubes, Carbon 80 (2014) 246–254.
[5] E. Frackowiak, Phys. Carbon materials for supercapacitor application, Chem. Chem. Phys. 9 (2009) 1774–1785.
[6] G. Wang, L. Zhang, J. Zhang, A review of electrode materials for electrochemical supercapacitors, Chem. Soc. Rev. 41 (2012) 797–828.
[7] Y.S. Yun, S.Y. Cho, J. Shim, B.H. Kim, S.J. Chang, S.J. Baek, Y.S. Huh, Y. Tak, Y.W. Park, S.J. Park, H.J. Jin, Microporous carbon nanoplates from regenerated silk proteins for supercapacitors, Adv. Mater. 25 (2013) 1993–1998.
[8] C. Merlet, B. Rotenberg, P.A. Madden, P.L. Taberna, P. Simon, Y. Gogotsi, M. Salanne, On the molecular origin of supercapacitance in nanoporous carbon electrodes, Nat. Mater. 11 (2012) 306–310.
[9] J. Huang, B.G. Sumpter, V. Meunier, Theoretical model for nanoporous carbon supercapacitors, Angew. Chem. Int. Ed. 47 (2008) 520–524.
[10] J. Huang, B.G. Sumpter, V. Meunier, A universal model for nanoporous carbon supercapacitors applicable to diverse pore regimes, carbon materials, and electrolytes, Chem. Eur. J. 14 (2008) 6614–6626.
[11] J. Chmiola, G. Yushin, Y. Gogotsi, C. Portet, P. Simon, P.L. Taberna, Anomalous increase in carbon capacitance at pore sizes less than 1 nanometer, Science 313 (2006) 1760–1763.
[12] L.L. Zhang, X.S. Zhao, Carbon-based materials as supercapacitor electrodes, Chem. Soc. Rev. 38 (2009) 2520–2531.
[13] A.G. Pandolfo, A.F. Hollenkamp, Carbon properties and their role in supercapacitors, J. Power Sources 157 (2006) 11–27.
[14] E. Raymundo-Piñero, K. Kierzek, J. Machnikowski, F. Béguin, Relationship between the nanoporous texture of activated carbons and their capacitance properties in different electrolytes, Carbon 44 (2006) 2498–2507.
[15] Y. Lv, F. Zhang, Y. Dou, Y. Zhai, J. Wang, H. Liu, Y. Xia, B. Tu, D. Zhao, A comprehensive study on KOH activation of ordered mesoporous carbons and their supercapacitor application, J. Mater. Chem. 22 (2012) 93–99.
[16] W. Xiong, M. Liu, L. Gan, Y. Lv, Y. Li, L. Yang, Z. Xu, Z. Hao, H. Liu, L. Chen, A novel synthesis of mesoporous carbon microspheres for supercapacitor electrodes, J. Power Sources 196 (2011) 10461–10464.
[17] J. Li, X. Wang, Q. Huang, S. Gamboa, P.J. Sebastian, Studies on preparation and performances of carbon aerogel electrodes for the application of supercapacitor, J. Power Sources 158 (2006) 784–788.
[18] M.D. Stoller, S. Park, Y. Zhu, J. An, R.S. Ruoff, Graphene-based ultracapacitors, Nano Lett. 8 (2008) 3498–3502.
[19] W. Wang, S. Guo, M. Penchev, I. Ruiz, K.N. Bozhilov, D. Yan, M. Ozkan, C.S. Ozkan, Three dimensional few layer graphene and carbon nanotube foam architectures for high fidelity supercapacitors, Nano Energy 2 (2013) 294–303.
[20] K. Xia, Q. Gao, J. Jiang, J. Hu, Hierarchical porous carbons with controlled micropores and mesopores for supercapacitor electrode materials, Carbon 46 (2008) 1718–1726.
[21] C. Liu, Z. Yu, D. Neff, A. Zhamu, B.Z. Jang, Graphene-based supercapacitor with

an ultrahigh energy density, Nano Lett. 10 (2010) 4863–4868.

[22] L. Zhao, L.Z. Fan, M.Q. Zhou, H. Guan, S. Qiao, M. Antonietti, M.M. Titirici, Nitrogen-containing hydrothermal carbons with superior performance in supercapacitors, Adv. Mater. 22 (2010) 5202–5206.

[23] W. Qian, F. Sun, Y. Xu, L. Qiu, C. Liu, S. Wang, F. Yan, Human hair-derived carbon flakes for electrochemical supercapacitors, Energy Environ. Sci. 7 (2014) 379–386.

[24] X. Ma, L. Gan, M. Liu, P.K. Tripathi, Y. Zhao, Z. Xu, L. Chen, Mesoporous size controllable carbon microspheres and their electrochemical performances for supercapacitor electrodes, J. Mater. Chem. A 2 (2014) 8407–8415.

[25] J. Mähler, I. Persson, A study of the hydration of the alkali metal ions in aqueous solution, Inorg. Chem. 51 (2011) 425–438.

[26] K. Fic, G. Lota, M. Meller, E. Frackowiak, Novel insight into neutral medium as electrolyte for high-voltage supercapacitors, Energy Environ. Sci. 5 (2012) 5842–5850.

[27] B. Xu, S. Hou, H. Duan, G. Cao, M. Chu, Y. Yang, Ultramicroporous carbon as electrode material for supercapacitors, J. Power Sources 228 (2013) 193–197.

[28] S.Y. Cho, Y.S. Yun, S. Lee, D. Jang, K.Y. Park, J.K. Kim, B.H. Kim, K. Kang, D.L. Kaplan, H.J. Jin, Dirac cones in two-dimensional conjugated polymer networks, Nat. Commun. 6 (2015) 5842.

[29] J. Romanos, M. Beckner, T. Rash, J. Firlej, B. Kuchta, P. Yu, G. Suppes, C. Wexler, P. Pfeifer, Nanospace engineering of KOH activated carbon, Nanotechnology 23 (2012) 015401.

[30] P.J.F. Harris, A. Burian, S. Duber, High-resolution electron microscopy of a microporous carbon, Phil. Mag. Lett. 80 (2012) 381–386.

[31] P.J.F. Harris, Impact of the discovery of fullerenes on carbon science, Chem. Phys. Carbon 28 (2003) 1–39.

[32] S.J. Townsend, T.J. Lenosky, D.A. Muller, C.S. Nichols, V. Elser, Negatively curved graphitic sheet model of amorphous carbon, Phys. Rev. Lett. 69 (1992) 921–924.

[33] A.L. Mackay, H. Terrones, Energetics of negatively curved graphitic carbon, Nature 352 (1991) 762.

[34] E. Bottani, J. Tascon, Adsorption by Carbon, Elsevier, Jordan Hill, Oxford, 2008.

[35] G. Beaucage, Approximations leading to a unified exponential/power-law approach to small-angle scattering, J. Appl. Cryst. 28 (1995) 717–728.

[36] G. Beaucage, Small-angle scattering from polymeric mass fractals of arbitrary mass-fractal dimension, J. Appl. Cryst. 29 (1996) 134–146.

[37] O.S. Kucheyev, M. Toth, T.F. Baumann, A.V. Hamza, J. Ilavsky, W.R. Knowles, C.K. Saw, B.L. Thiel, V. Tileli, T.V. Buuren, Y.M. Wang, T.M. Willey, Structure of low-density nanoporous dielectrics revealed by low-vacuum electron microscopy and small-angle X-ray scattering, Langmuir 23 (2007) 353–356.

[38] D. Hulicova-Jurcakova, M. Seredych, G.Q. Lu, T.J. Bandosz, Combined effect of nitrogen- and oxygen-containing functional groups of microporous activated carbon on its electrochemical performance in supercapacitors, Adv. Funct. Mater. 19 (2009) 438–447.

[39] Y.S. Yun, D.H. Kim, S.J. Hong, M.H. Park, Y.W. Park, B.H. Kim, H.J. Jin, K. Kang, Microporous carbon nanosheets with redox-active heteroatoms for pseudocapacitive charge storage, Nanoscale 7 (2015) 15051–15058.

[40] Y.S. Yun, M.E. Lee, M.J. Joo, H.J. Jin, High-performance supercapacitors based on freestanding carbon-based composite paper electrodes, J. Power Sources 246 (2014) 540–547.

[41] Z. Lei, N. Christov, X.S. Zhao, Intercalation of mesoporous carbon spheres between reduced graphene oxide sheets for preparing high-rate supercapacitor electrodes, Energy Environ. Sci. 4 (2011) 1866–1873.

[42] Z. Lei, Z. Liu, H. Wang, X. Sun, L. Lu, X.S. Zhao, A high-energy-density supercapacitor with graphene–CMK-5 as the electrode and ionic liquid as the electrolyte, J. Mater. Chem. A 1 (2013) 2313–2321.